Parameterization of Prismatic Lithium-Iron-Phosphate Cells through a Streamlined Thermal/Electrochemical Model

Howie N. Chu[a,†], Sun Ung Kim[b,d,†], Saeed Khaleghi Rahimian[c,†], Jason B. Siegel[d], and Charles W. Monroe[a,z]

[a] *Department of Engineering Science, University of Oxford, Oxford OX13PJ, United Kingdom*

[b] *School of Engineering and Computer Science, Washington State University, Vancouver, WA, 98686, United States*

[c] *Department of Chemical Engineering, University of Michigan, Ann Arbor 48109, United States*

[d] *Department of Mechanical Engineering, University of Michigan, Ann Arbor 48109, United States*

[z] Corresponding author: charles.monroe@eng.ox.ac.uk

[†]These authors contributed equally to the theory and model implementation. Mr Chu designed, implemented, and analyzed the experiments.

Abstract

A model is proposed and used to parameterize the surface-temperature distribution and electrical response for A123 20 Ah $LiFePO_4$ prismatic cells. The cell interior is described by a porous-electrode charge-transport model based on Newman–Tobias theory, which is coupled to a local heat balance. Simulation output depends on only a few observable dimensionless quantities, allowing parameter estimation *via* iterative optimization schemes that directly compare computed results with experimental voltage and surface-temperature measurements. Despite the neglect of mass-transport limitations within Newman–Tobias theory, the model accurately predicts the dynamic terminal voltage, as well as the minimum, maximum, and surface-averaged temperature on the cell exterior. The electrochemical and thermal properties extracted from square-wave cycling data with various excitation amplitudes (2 C and 4 C) and short charge/discharge periods (50 s and 100 s) compare well with literature values, showing that it is possible to infer internal material properties by fitting external measurements. The temperature dependence of parameters has clear signatures in the observed voltage.

1. Introduction/Motivation

Owing to their large energy densities and low packaging cost, large-format prismatic Li-ion cells are becoming ubiquitous. Among large-format cells, prismatic pouch cells are one of the most widely used types. One might think that thermal management would be easier for cells with large surface-to-volume ratios, but several researchers have reported that the temperature distributions across prismatic cells can be significantly non-uniform, which can severely impact their performance [1–5]. Figure 1 presents infrared thermography images of 20 Ah prismatic pouch cells that exhibit such non-uniformity, with higher temperatures near the tabs. Even if such 'hot spots' do not cause catastrophic cell failure, inhomogeneities in temperature during cycling lead to a non-uniform thermal history within a battery, which may affect its cycle life [6,7]. Thus accurate health and performance models require detailed understanding of how cell materials and chemistry impact temperature distributions.

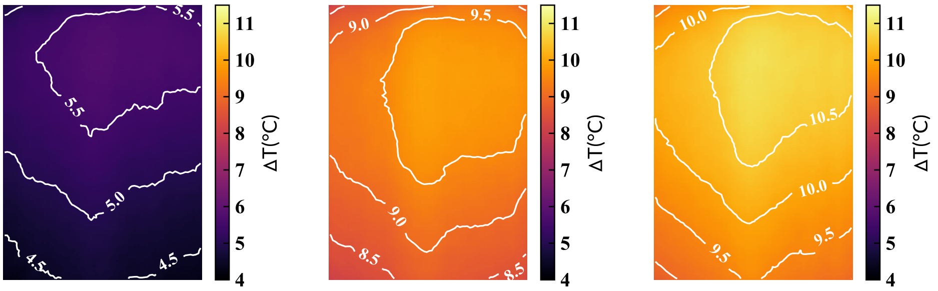

Figure 1 Three infrared images ($\Delta T = T - T_\infty$) of the surface of a 20 Ah lithium-ion battery cell, under 4 C charge-discharge cycling with 100 s period, freely hanging in stagnant air with T_∞ = 25 °C. To illustrate how surface temperature develops, the images show the temperature of an initially isothermal battery after (a) 5 minutes, (b) 20 minutes, and (c) 45 minutes of continuous cycling.

When performing electrochemical/thermal modeling, one must consider the possible coupling of heat and charge transport. The approach to modeling heat transfer is common across groups, but there are two distinct philosophies of charge-transport modeling: equivalent-circuit modeling (ECM) [8–12] and physics-based electrochemical mass-transport modeling [13–26]. Both methods describe the terminal-voltage response of Li-ion battery cells quite accurately, but their levels of detail regarding the material properties of cell constituents differ significantly. Since battery temperature impacts phenomena like mechanical fatigue, side reactions, and other factors associated with aging, it is worthwhile to develop electrothermal models that incorporate material properties. On the other hand, it is desirable to develop simulations that keep computational complexity at a minimum, both to increase the utility of models for battery-management applications and to facilitate iterative model-parameterization schemes.

Fleckenstein *et al.* modeled a battery cell as an aggregate of volume elements through which charge transport is described by equivalent circuits, coupling these to a general energy balance that accounts for local heat accumulation, conduction, and generation [27]. The charge balance communicates irreversible Joule heating and reversible reaction heat into the local thermal-energy balance. Also, the thermal model in principle communicates back to the equivalent circuits, through functions that establish the temperature dependences of resistances and capacitances. Although it was found to match experimental temperature-distribution data effectively for a 32113-type 4.4 Ah $LiFePO_4$ (LFP cathode) battery, the model of Fleckenstein *et al.* has the same limitations as other ECMs: it is not clear how the resistances and capacitances involved in the equivalent circuits relate to the physical properties of materials and interfaces within the cell.

Electrochemical mass-transport models [13–21] have also been used to underpin thermoelectrochemical simulations. The now-standard Dualfoil scheme developed by Fuller, Doyle, and Newman is the most commonly used mechanistically based electrochemical model [14–16]. Dualfoil augments the Newman–Tobias porous-electrode theory [20] by accounting for concentration polarization in the separator, pore-filling electrolyte, and solid intercalation media. The original form of Dualfoil combined porous-electrode theory, concentrated-solution theory, and intercalation dynamics in the solid phase.

Bernardi *et al.* explored the thermal management problem, under the assumption that the temperature within a cell is locally uniform [28]. Srinivasan and Wang [21] provided the most complete coupling of Dualfoil to a local heat balance. They solved the electrochemical and thermal model equations simultaneously by discretizing the partial differential equations involved and using an implicit linear multistep solution method. Prada *et al.* developed a pseudo-two-dimensional thermoelectrochemical model for LFP cells [25]. A simplified electrochemical model (modified single-particle model) was coupled to Forgez *et al.*'s analytical solution of the temperature distribution in the cylindrical system [29] to reduce computational costs.

Recently, Christensen *et al.* suggested a new approach for three-dimensional thermoelectrochemical modeling, which was applied to 18650 Nickel Manganese Cobalt Oxide (NMC) lithium-ion cells [13] and larger 50 Ah automotive lithium-ion batteries [17]. Under an assumption that Soret/Dufour diffusion is negligible, the thermal and electrochemical models can be partially decoupled, allowing the electrochemical and thermal problems to be solved sequentially at a given timestep. This approach permits the battery interior to be described with two different spatial meshes, with differing mesh spacings appropriate to the electrochemical and thermal problems. In order to decrease computation time, sparser meshing was adopted for the electrochemical description.

This paper aims to describe the non-uniform thermal response of large-format prismatic LFP pouch cells using a microscopic electrothermal model that has computational efficiency comparable to an ECM, while still retaining some of the insight about material properties that Dualfoil provides. This objective is achieved by describing mass and charge transport within the battery through a simpler perspective provided by the original Newman–Tobias porous-electrode theory, while describing heat transfer through the more detailed perspectives of Srinivasan and Wang or Christensen *et al.*

The streamlined model put forward here can be solved relatively quickly with the COMSOL finite-element package, which enables multi-objective parameterization schemes based on direct processing of spatially resolved experimental lock-in thermography data. The complete electrochemical/thermal simulation is run iteratively to target parameters that minimize the difference between model predictions and experimental data describing the dynamic cell voltages and surface-temperature distributions of large-format prismatic LFP pouch cells. Although the proposed model is much simpler than Dualfoil, we find that it suffices to match the minimum, maximum, and surface-average temperatures during short-period charge/discharge experiments, as well as matching the dynamic output voltage of the cell. Finally, the parameters yielded by the optimization scheme can be analyzed to provide insight into the microscopic physics that control the battery's electrochemical and thermal response.

2. Experimental

Several of the fundamental properties of a battery depend on its state of charge (SOC) [30–35]. Therefore, a control scheme involving short-duration charges and discharges with fixed periodicity was introduced to allow the study of rate and temperature effects without inducing significant changes in the volume-averaged thermodynamic state. Square-wave excitation tests with variable wave amplitude A and period p were performed around various average SOCs, such as 30 % and 50 %. Around 50 % SOC, the open-circuit potential (OCP) of the A123 battery used for experiments exhibits a plateau (or linear characteristics with very small gradient) with respect to charge state, further ensuring that the properties are relatively constant. After determining the SOC swing induced by the input signal, the initial battery SOC was offset in such a way that the average state during the excitation centered around the SOC of choice. For example, for the $A = 4$ C and $p = 100$ s square wave, the charge portion of the signal increases the SOC by 5.56 %. To keep the mean SOC at 30 % during the cycling, the battery was initially equilibrated at an SOC of 30–5.56/2 = 27.22 %. To set its initial state, the cell was charged with a constant current, constant voltage (CCCV) protocol until fully charged (3.6 V until current decays to C/100), and then discharged to the desired starting state by coulomb counting, using the manufacturer-specified 20 Ah as the assumed charge capacity. The cell was then left to rest for 2-3 hours until both voltage and surface temperature had equilibrated before starting the thermography experiment.

An apparatus was designed to hold batteries without impeding their ability to dissipate heat by natural convection. Specifically, a prismatic cell needs to be held such that its large front and back surfaces are not impeded by any thermal insulation (such as occurs when a cell is placed on top of a table or bench). Traditionally, alligator clips are used to make electrical connections, but this was found to create substantial contact resistance, leading to the generation of extraneous heat that led to systematic experimental error and irreproducibility. Some groups avoid the contact resistance of alligator clips by cutting holes in the battery tabs and securing electrical connections with nuts and bolts. This permanently changes the tab geometry and can make operating temperature higher by reducing the amount of conductive tab materials.

While designing the cell holder, it was decided that the battery tabs should be left pristine and connected to the power supply *via* copper bars (McMaster-Carr Super-Conductive Copper Bars) with high thermal masses. These bars contained holes that allowed the potentiostat leads to be connected with nuts and bolts. The battery tabs were pressed against the opposite ends of the copper bars and held in place with silicone rubber (McMaster-Carr High-Temperature Silicone Rubber). Machined nylon sheets (McMaster-Carr Nylon Grade 6) were used to enclose both the copper bars and the silicone rubber. Nylon sheets are good electrical insulators and are safe to use over a large range of temperatures. Finally, an acrylic sheet (McMaster-Carr Clear Cast Acrylic) was cut and assembled into a frame that could support the weight of the vertically orientated battery, while not impeding the ability of its largest faces to dissipate heat by free convection. The assembled acrylic holder was attached to a metal frame. Figure 2 shows schematics of the individual components; Figure 3a shows a photograph of the assembled frame.

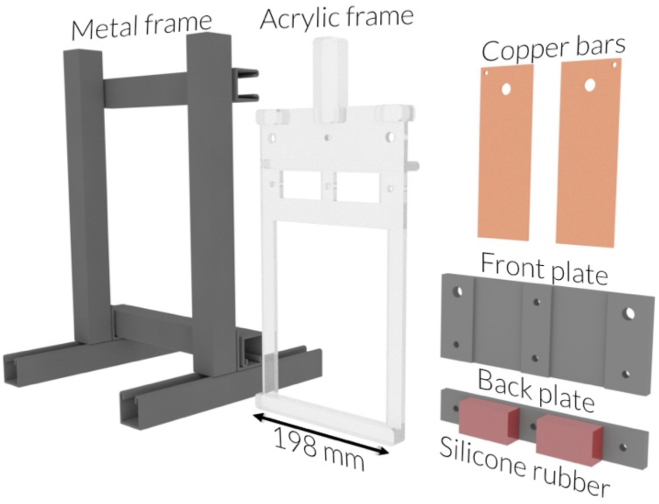

Figure 2 Individual components of prismatic battery holder

While the battery was subjected to AC excitations, surface-temperature profiles were measured with an infrared (IR) camera (FLIR A35sc). The tests were performed on 20 Ah LFP pouch cells from A123 Inc. Figure 3c shows the IR camera setup: the camera was placed sufficiently far from the battery to be at a distance greater than the minimum focal distance, and also far enough so that auxiliary components (copper bars, ambient spot, reflector) were within frame – in practice, this distance was about 0.75 m. Krylon ultra-flat black paint was applied to the battery surface to establish a uniform emissivity of 0.95 ~ 0.97. Because of the long focal length of the IR camera lens, thermography experiments could not be performed inside a temperature-controlled chamber. Instead, the experiments were conducted in an isolated room with stable ambient temperature controlled by exterior air conditioning.

An 'ambient spot', comprising a piece of black felt held up by a thermocouple, was used to help mitigate errors associated with IR thermography, which generally measures relative temperature very precisely, but is susceptible to more error in absolute temperature. The ambient spot is visible on the right of the battery cell in figure 3c. All reported IR temperature data was post-processed by taking the average temperature of the region of interest and subtracting the average temperature across the ambient spot, to reduce noise and remove temperature jumps caused by the IR sensor recalibrating during an experiment. The temperature read by the thermocouple – which measures absolute temperature more precisely – was added back to the relative temperatures from IR to establish the absolute temperature across the battery surface.

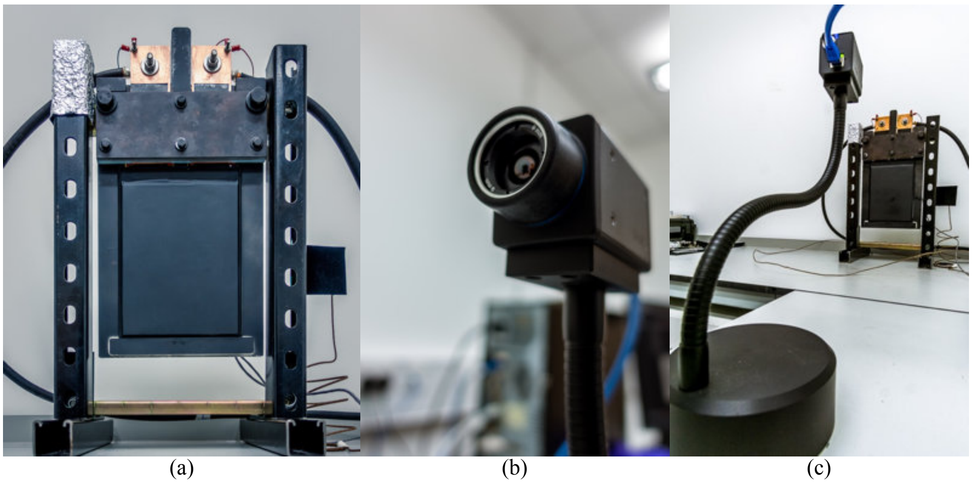
(a) (b) (c)

Figure 3 (a) Assembled battery holder with prismatic cell and (b) FLIR A35sc camera. (c) Completed experimental setup.

The rightmost image of figure 1 shows a representative temperature measurement from the IR camera after 50 minutes of square-wave excitation with A = 4 C and p = 100 s (abbreviated as 4c100s). One would expect irreversible Joule heating during the excitation; the square-wave excitation was chosen because it keeps the rate of Joule heating more constant than a sinusoid. Power scales as I^2R, and I has the same magnitude despite its switch in sign. Any oscillations in temperature in the periodic steady state can therefore be more readily attributed to reversible heating. The surface temperature is non-uniform during the excitation tests; thus additional factors contribute to the thermal response of these prismatic cells.

Typical transient voltage and temperature data in response to a square-wave excitation are shown in figure 4. The cell responses were characterized by observing several key features of the voltage and temperature profiles once the system reached a periodic steady state; these features are labelled in figure 4 as well. The alternating electric current generates a corresponding output voltage which has a maximum variation ΔV_{T}. Unlike the input current, the output voltage profile does not follow a square wave but exhibits transient relaxations; the transients are described by tracing the magnitude of the voltage increase during the charge step, ΔV_{chrg}, and the voltage relaxation's characteristic time constant, $t_{V_{\mathrm{chrg}}}$. The value of $t_{V_{\mathrm{chrg}}}$ is identified by finding the time after the step begins when the voltage has relaxed across 50% of ΔV_{chrg}.

Figure 4b shows the evolution of minimum, maximum, and surface temperatures on the battery surface in the periodic steady state. Thermal oscillations are observed, implying that heat absorption occurs at some points as the SOC swings. Such behavior is ascribed to the reversible heat – that is, the entropy – of the cell reaction, which can act as a heat source or sink depending on the sign of the current and the SOC. The maximum temperature fluctuation in the periodic steady state, ΔT_{fluc}, is also noted as a characteristic feature and used for parameterization. Reaction entropy has been quantified for a number of battery systems and electrode materials [31–34,36]. The non-uniformity of the temperature profile is quantified by taking the difference between the time-averaged maximum temperature and the time-averaged mean temperature, $\langle T_{\mathrm{max}} \rangle - \langle T_{\mathrm{avg}} \rangle$.

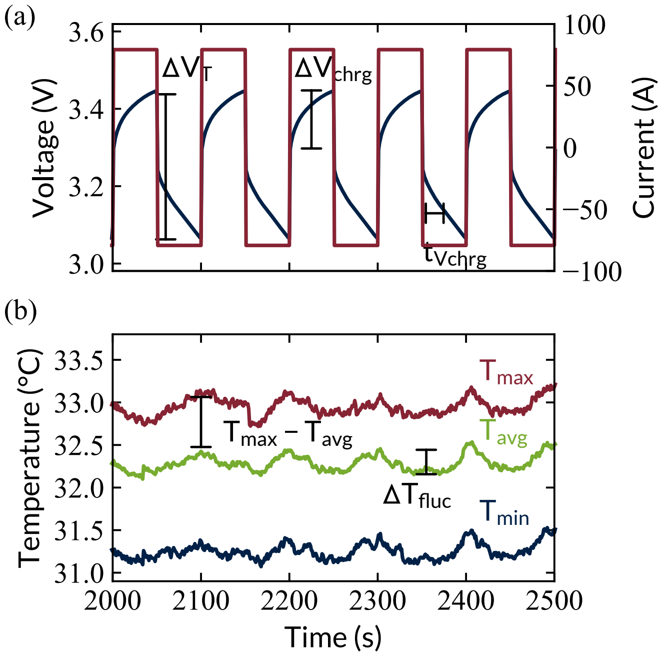

Figure 4 General (a) electrical and (b) thermal responses to AC square-wave current. Characteristic features used for sensitivity testing of the thermoelectrochemical model are labelled on the figures.

3. Modeling

3.1 Newman–Tobias Theory (Electrical Porous-Electrode Theory)

The Newman–Tobias model [20] neglects concentration polarization, describing charge transport within porous electrodes from a purely electrical standpoint. A ‘macrohomogeneous approach’ is taken, in which the microscopic geometry of porous materials is described by a local porosity ε and surface-to-volume ratio a_V. Newman and Tobias originally analyzed the steady-state current, potential, and reaction distributions in planar porous electrodes with both linear and Tafel interfacial kinetics under isothermal conditions [20]. They identified a few key dimensionless parameters that govern the charge distribution and reaction distribution within porous electrodes. The Newman–Tobias model is computationally much more efficient than Dualfoil, and, when coupled to an energy balance, provides enough parameters to match all of the characteristics of the responses labeled in figure 4, despite the neglect of concentration polarization.

Each volume element of the electrodes comprises two phases that allow charge transport – electrically conductive solid and ionically conductive liquid – which also permit charge exchange through local interfacial reactions. Dynamic charge balances on the solid and liquid phases, which are designated with subscripts sol and liq, respectively, take the form

$$\vec{\nabla} \cdot \vec{\imath}_{\mathrm{sol}} = -a_V \mathrm{i}_{\mathrm{k}} \tag{1}$$

$$\vec{\nabla} \cdot \vec{\imath}_{liq} = a_V i_{\mathrm{k}}. \tag{2}$$

Note that overall charge conservation within each volume element implies that the sum of these currents is solenoidal, $\vec{\nabla} \cdot \left(\vec{\imath}_{\mathrm{sol}} + \vec{\imath}_{\mathrm{liq}}\right) = 0$. The generation terms in equations (1) and (2) account for the kinetic current i_{k}, which expresses the charge flux across the liquid/solid interface within a volume element due to electrochemical reactions. Generally, the bulk-liquid and solid current densities $\vec{\imath}_{\mathrm{liq}}$ and $\vec{\imath}_{\mathrm{sol}}$ are positive when anodic; positive current associated with interfacial charge exchange, i_{k}, flows into the solid from the electrolyte.

Since the LFP chemistry has been observed to exhibit relatively high exchange-current densities, the kinetic current was described using linear kinetics, as

$$\rho_{\mathrm{k}} i_{\mathrm{k}} = a_V \left(\Phi_{\mathrm{sol}} - \Phi_{\mathrm{liq}} - \mathrm{U}\right), \tag{3}$$

in which a_V is the surface-area-to-volume ratio, Φ_{sol} and Φ_{liq} are the potentials in the solid and electrolyte phases, U is the open-circuit potential (OCP), and ρ_{k} is the kinetic resistivity. Here the kinetic resistivity relates to the interfacial exchange-current density i_0 through

$$\frac{1}{\rho_{\mathrm{k}}} = \frac{i_0 n F}{a_V R T} \tag{4}$$

where n is the number of charges involved in the half reaction, F is Faraday's constant, R is the gas constant, and T is the absolute temperature. Note that equation (4) illustrates an explicit first-order dependence on inverse temperature, but the exchange-current density also generally is observed to have an Arrhenius temperature dependence. It is worth noting that nonlinear (Butler–Volmer) current-voltage relations were tried in place of equation (3), but did not make a substantial impact on simulation results; the linear form was therefore retained because it made convergence of the model faster.

During the square-wave excitation tests, the period and amplitude of the signal were chosen such that the overall charge state did not vary more than a few percent. Owing to the small variation, one can assume that the perturbation in SOC induced by the input signal induces a more or less linear response in equilibrium potential, so that

$$U = U_0 + k_U q + V_{\mathrm{hys}} \cdot \mathrm{sgn}(i_{\mathrm{k}}). \tag{5}$$

Here q is the local SOC in the volume element; k_U expresses the gradient of the OCP with respect to SOC at the average SOC, and U_0 is the OCP at the average SOC. Note that the assumption of a linearized equilibrium-voltage response is justified on a global level, but may lead to some errors on a local level, because some domains of the electrode may experience much wider swings in SOC than others. This issue did not appear to impact the effectiveness of the parameterization substantially, however.

The LFP chemistry is also known to exhibit equilibrium-voltage hysteresis. Depending on how the battery has reached a certain SOC (*via* charge or discharge), the corresponding voltage may differ. Figure 5 presents pseudo-OCV data for the A123 20 Ah LFP battery, obtained by charging and discharging at a C/25 rate. In the range of SOC that we are presently concerned with, the two curves are offset from each other by a fixed amount (the inset in Figure 5 shows a zoomed in view of the relevant region for these thermography experiments). The offset in charge and discharge in this region is 0.04 V. To account for this in a simple manner, the offset was split evenly; 0.02 V is added to the OCP during charge and 0.02 V is subtracted from the OCP during discharge. This is represented by the $V_{\mathrm{hys}} \cdot \mathrm{sgn}(i_{\mathrm{k}})$ term of equation (5).

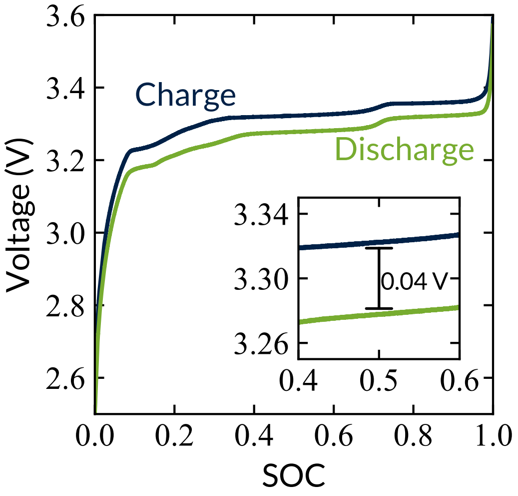

Figure 5 Pseudo-OCV curves for the A123 20 Ah cell at 25 °C, generated by galvanostatic cycling at C/25.

The local SOC q on which U depends is dimensionless, and is bounded between 0 and 1. It relates to the local kinetic current i_k and the maximum capacity density of the electrode Q_{max} through

$$\frac{\partial q}{\partial t} = \frac{a_V i_k}{Q_{\mathrm{max}}}. \qquad (6)$$

Finally, following Newman and Tobias, Ohm's law is adopted in each phase to relate the local current densities to the gradients of potential,

$$\vec{\nabla}\Phi_{\mathrm{sol}} = -\rho_{\mathrm{sol}}\vec{i}_{\mathrm{sol}}, \qquad (7)$$

$$\vec{\nabla}\Phi_{\text{liq}} = -\rho_{\text{liq}}\vec{i}_{\text{liq}}, \tag{8}$$

where ρ_i is the resistivity of the phase i. Equations (1)-(8) comprise a general statement of the model used to describe electrode domains in this work. The overall computational cost is much lower than models that include mass diffusion effects, allowing iterative 3-D simulations to be implemented for model parameterization.

3.2 General energy balance

A local energy balance was coupled to electrical governing equations (1)-(8). The general form of this balance for a single, stationary, isobaric, multicomponent phase is [37]

$$C_{p,\text{eff}}\frac{\partial T}{\partial t} = -\vec{\nabla}\cdot\left(-k_{\text{eff}}\vec{\nabla}T + \sum_i \bar{H}_i\vec{J}_i + \vec{q}^{(x)}\right) + \sum_i \bar{H}_i\left(\vec{\nabla}\cdot\vec{J}_i - R_i\right) \tag{9}$$

where $C_{p,\text{eff}}$ is the volumetric constant-pressure heat capacity, k_{eff} is the thermal conductivity, and $\vec{q}^{(x)}$ is the Dufour energy flux density; $\bar{H}_i$, $\vec{J}_i$, and R_i are the partial molar enthalpy, molar flux density relative to the mass-average velocity, and homogeneous generation rate of species i, respectively.

Neglecting the Dufour flux [32–34] and applying the thermodynamic definition of the partial molar enthalpy, Faraday's law and Ohm's law simplify equation (9) to

$$C_{p,\text{eff}}\frac{\partial T}{\partial t} = k_{\text{eff}}\nabla^2 T + \vec{\nabla}k_{\text{eff}}\cdot\vec{\nabla}T + \frac{1}{\rho_{\text{sol}}}\left\|\vec{\nabla}\Phi_{\text{sol}}\right\|^2 + \frac{1}{\rho_{\text{liq}}}\left\|\vec{\nabla}\Phi_{\text{liq}}\right\|^2 + \rho_{\text{k}}i_k^2 - \frac{a_V T\Delta\bar{S}_{rxn}}{nF}i_k, \tag{10}$$

where $\Delta\bar{S}_{\text{rxn}}$ is the local reaction entropy. The right side of equation (10) accounts for thermal conduction and contains four heat-generation terms, including Joule heats associated with each phase in the porous electrode, Joule heating associated with interfacial charge transfer, and reversible heat generation associated with reaction entropy. Use of equation (10) assumes that the solid and liquid phases within a volume element of a porous electrode are in local thermal equilibrium; the heat capacity and thermal conductivity that appear should be interpreted as effective properties of the mixed phases.

In accordance with the experimental setup, a convective boundary condition is used at the external surfaces of the cell,

$$h(T - T_\infty) = -k_{\mathrm{eff}} \vec{\nabla} T \cdot \vec{n} \tag{11}$$

Here h is an interfacial heat-transfer coefficient and $\vec{n}$ is a unit vector normal to the surface pointing outward.

Equations (1)-(8) combine with equation (10) to simulate the coupling between electric and thermal phenomena in a porous electrode. Note that even this ostensibly ‘simple’ formulation of the electrothermal porous-electrode transport model and its associated boundary conditions contains many parameters. It is already difficult to see what properties affect the system response, and in what ways.

4. Dimensional Analysis

4.1 Non-dimensionalization

Newman and Tobias [20] provided a compact set of dimensionless parameters that control the charge distribution and reaction distribution within a porous electrode at steady state. In this section, their dimensional analysis is expanded to analyze the transient thermal response. Dimensional analysis of the equation system reveals that the physics is governed by the control parameters

$$I = \frac{i_{\mathrm{app}}}{i_0 a_V \delta} = i_{\mathrm{app}} \frac{\rho_k}{a_V^2 \delta} \frac{nF}{RT_\infty}, \text{ and } Bi = \frac{h \delta_{\mathrm{T}}}{k_{\mathrm{eff}}} \tag{12}$$

and the material properties

$$\begin{gathered} \mathrm{P}_{\mathrm{sol}} = \frac{\rho_{\mathrm{sol}}}{\rho_{\mathrm{k},\infty}} a_V^2 \delta^2, \ \mathrm{P}_{\mathrm{liq},\infty} = \frac{\rho_{\mathrm{liq}}}{\rho_{\mathrm{k},\infty}} a_V^2 \delta^2, \ \mathrm{P}_{\mathrm{cc}} = \frac{\rho_{\mathrm{cc}}}{\rho_{\mathrm{k},\infty}} a_V^2 \delta^2, \\ H = \frac{n^2 F^2 \rho_{\mathrm{k},\infty} h}{R^2 T_\infty a_V^2 \delta_{\mathrm{T}}}, \ \sigma = \frac{\Delta \bar{S}_{\mathrm{rxn}}}{R}, \\ K_U = \frac{nF}{RT_\infty} k_U, \text{ and } \bar{Q}_{\mathrm{max}} = \frac{Q_{\mathrm{max}}}{C_{\mathrm{p,eff}}} \frac{R}{nF}. \end{gathered} \tag{13}$$

The control parameters I and Bi are dimensionless applied current and Biot number, respectively. Material characteristics are embodied by, $\mathrm{P}_{\mathrm{sol}}$, $\mathrm{P}_{\mathrm{liq}}$, and P_{cc}, which are the ratios of the porous-electrode solid, porous-electrode liquid, and current-collector resistivities to kinetic resistivity, respectively. The thermal parameter H expresses the ratio between the rate of heat dissipation and the characteristic rate of heat generation by the electrochemical reaction. σ is the dimensionless entropy of reaction, K_U is the dimensionless OCP gradient, and $\bar{Q}_{\mathrm{max}}$ expresses the relative magnitudes of charge capacity and heat capacity.

The control parameter and material properties determine relationships between the dimensionless positions ξ_x, ξ_y, and ξ_z, dimensionless time τ, the solid- and liquid-phase voltages ϕ_{sol} and ϕ_{liq}, current collector voltage ϕ_{cc}, the dimensionless surface overpotential ι_{k}, and the temperature distribution θ. The independent variables are defined as

$$\xi_{\mathrm{x}} = \frac{x}{\delta}, \xi_y = \frac{y}{L_y}, \xi_z = \frac{z}{L_z}, \text{and } \tau = \frac{ht}{C_{p,\mathrm{eff}}\delta_T} \tag{14}$$

and the dependent variables are

$$\begin{gathered} \phi_{\mathrm{sol}} = \frac{nF\Phi_{\mathrm{sol}}}{RT_\infty}, \phi_{\mathrm{liq}} = \frac{nF\Phi_{\mathrm{liq}}}{RT_\infty}, \phi_{\mathrm{cc}} = \frac{nF\Phi_{\mathrm{cc}}}{RT_\infty}, \\ \iota_{\mathrm{k}} = \frac{\rho_{k,\infty} i_k}{a_V}\frac{nF}{RT_\infty}, \text{and } \theta = \frac{T}{T_\infty}. \end{gathered} \tag{15}$$

Here x is the direction normal to the stacked electrodes; y and z are directions in the plane of the electrode. δ, δ_{T}, L_y, and L_z are the electrode thickness, total thickness, width of the battery, and length of the battery, respectively.

Incorporating the dimensionless quantities in equations (12)-(15) and defining the dimensionless gradient operator $\vec{\nabla}^*$ as

$$\vec{\nabla}^* = \vec{e}_x \frac{\partial}{\partial \xi_{\mathrm{x}}} + \vec{e}_y \frac{\delta}{L_y}\frac{\partial}{\partial \xi_y} + \vec{e}_z \frac{\delta}{L_z}\frac{\partial}{\partial \xi_z}\,. \tag{16}$$

governing equations (1)-(8) become

$$\nabla^{*2}\phi_{\mathrm{sol}} = \iota_{\mathrm{k}} P_{\mathrm{sol}}, \tag{17}$$

which describes the solid phase of the porous electrodes,

$$\nabla^{*2}\phi_{\mathrm{liq}} - \frac{d\ln\tilde{\rho}_{\mathrm{liq}}}{d\theta}\left(\vec{\nabla}^*\theta \cdot \vec{\nabla}^*\phi_{\mathrm{liq}}\right) = -\iota_{\mathrm{k}} P_{\mathrm{liq},\infty}\tilde{\rho}_{\mathrm{liq}}, \tag{18}$$

which describes the liquid phase, and

$$\nabla^{*2}\phi_{\mathrm{cc}} = 0, \tag{19}$$

which describes the current collector. To decrease computational cost several governing equations were combined analytically. To get equations (17) and (18), equations (1) and (2) were inserted to equations (7) and (8) and then nondimensionalized. Laplace's equation can be used to describe the voltage in the current collectors, which comprise only a single phase, whose parameters are independent of temperature.

At the top of the tabs, the applied electric current gives the following flux boundary condition:

$$-\vec{\nabla}^{*}\phi_{\mathrm{cc}}\cdot\vec{n} = \mathrm{P}_{\mathrm{cc}}I. \tag{20}$$

The superscript cc represents the current collector. The change of local SOC was also nondimensionalized to

$$\frac{\partial q}{\partial \tau} = \frac{1}{\bar{Q}_{\mathrm{max}}H}\iota_{\mathrm{k}}. \tag{21}$$

Energy equation (10) takes the dimensionless forms

$$\frac{\partial \theta}{\partial \tau} = \frac{1}{Bi}(\nabla^{*2}\theta) + \frac{1}{H}\left\{\frac{1}{P_{\mathrm{sol}}}\left\|\vec{\nabla}^{*}\phi_{\mathrm{sol}}\right\|^{2} + \frac{1}{P_{\mathrm{liq},\infty}\tilde{\rho}_{\mathrm{liq}}}\left\|\vec{\nabla}^{*}\phi_{\mathrm{liq}}\right\|^{2} + \tilde{\rho}_{\mathrm{k}}\iota_{\mathrm{k}}^{2} + \sigma\theta\iota_{\mathrm{k}}\right\} \tag{22}$$

$$\hat{C}_{p,cc}\frac{\partial \theta}{\partial \tau} = \hat{k}_{\mathrm{cc}}\frac{1}{Bi}(\nabla^{*2}\theta) + \frac{1}{H}\frac{1}{\mathrm{P}_{\mathrm{cc}}}\left\|\vec{\nabla}^{*}\phi_{\mathrm{cc}}\right\|^{2} \tag{23}$$

in the porous electrode and current collector, respectively. Note that in the current collector, the generation term includes only Joule heating. The expressions are complicated somewhat because properties depend on temperature – parameters $\tilde{\rho}_{\mathrm{liq}}$ and $\tilde{\rho}_{\mathrm{k}}$ represent the ratio between the respective resistivities evaluated at local temperature T and T_{∞}. Since the thermal properties in the current collector differ from the active materials in the cell, $\hat{C}_{p,\mathrm{cc}}$ and $\hat{k}_{\mathrm{cc}}$ are introduced to represent the ratio between the respective parameter values in the current collector and those in the porous electrode. Finally, the convective boundary condition at all the external surfaces, equation (11), nondimensionalizes to

$$\mathrm{Bi}(\theta - 1) = -\vec{\nabla}^{*}\theta\cdot\vec{n}. \tag{24}$$

4.2 Scaling laws for multilayer cells

The number of consecutive electrochemical-cell-sandwich layers in the cell was estimated as $N = 40$, based on the thickness of an unwound electrode measured with calipers. Because the current collectors are coated on both sides, the number of physical layers is 20. To reduce the computational burden, only one layer of electrodes and current collectors with the thickness of 40 times larger than the actual thickness was simulated ($\delta_1 = \delta_N \times N$). To attain the same electrochemical/thermal response on the N-layer cell, all dimensionless numbers were required to be identical across the cell domain as well as at the boundaries.

Since the N-layer cell has N times the total surface area of one layer, the current density of a N-layer cell is $\frac{1}{N}$ of that layer cell, however, the thickness will be also be $\frac{1}{N}$ of the one-layer cell's, $\delta_N = \frac{\delta_1}{N}$. Thus, equation (12) implies that the ratio between kinetic resistivity and the square of surface-to-volume ratio does not change in a one-layer cell:

$$I_1 = I_N \colon \frac{i_{\mathrm{app},1}\rho_{\mathrm{k},1}}{\delta_1 a_{V,1}^2}\frac{nF}{RT} = \frac{i_{\mathrm{app},N}\rho_{\mathrm{k},N}}{\delta_N a_V^2}\frac{nF}{RT} \colon$$

$$\frac{i_{\mathrm{app},1}}{\delta_1}\left(\frac{\rho_{\mathrm{k}}}{a_V^2}\right)_1 = \frac{i_{\mathrm{app},1}/N}{\delta_1/N}\left(\frac{\rho_{\mathrm{k}}}{a_V^2}\right)_N \colon \left(\frac{\rho_{\mathrm{k}}}{a_V^2}\right)_1 = \left(\frac{\rho_{\mathrm{k}}}{a_V^2}\right)_N .$$

To make the dimensionless numbers $\mathrm{P}_{\mathrm{sol}}$, $\mathrm{P}_{\mathrm{liq}}$, and P_{cc} in equation (13) invariant between one-layer and N-layer cells, the respective resistivities in one layer need to be multiplied by a factor of N^2:

$$\mathrm{P}_{\mathrm{sol},1} = \mathrm{P}_{\mathrm{sol},1} \colon \left(\frac{a_V^2}{\rho_k}\right)_1 \rho_{sol,1}\delta_1^2 = \left(\frac{a_V^2}{\rho_k}\right)_N \rho_{sol,N}\delta_N^2 \colon$$

$$\rho_{sol,1}\delta_1^2 = \rho_{sol,N}\,\delta_1^2/N^2 \colon \rho_{sol,1}N^2 = \rho_{sol,N}$$

Other parameters, including thermal conductivity, heat transfer coefficient, reaction entropy, OCP gradient and heat capacity do not need to change to leave the dimensionless numbers $I, \mathrm{Bi}, \sigma, K_{\mathrm{U}}$, and τ invariant. We applied the above parameter scaling and used simulations to confirm that the global thermal and electrochemical responses were identical for one-layer, two-layer, and four-layer cells.

5. Model Implementation and Parameter Estimation

COMSOL Multiphysics commercial software was used to implement finite-element numerical analysis. The generic partial-differential-equation solver in COMSOL was used to implement the model equations stated above. Fitting parameters were determined by varying key dimensional material properties, such as $\Delta\bar{S}_{\mathrm{rxn}}$ to vary σ, ρ_{sol} to vary $\mathrm{P}_{\mathrm{sol}}$, and so on. Geometric parameters and solid-phase conductivities were taken from measurements or literature [21,25,38–42].

The OCP of the cathode (LFP) is effectively linear with a low rate of change for multiple wide ranges of SOCs [25]. The gradient of the OCP with respect to SOC (k_U) was estimated by taking the derivative of measured pseudo-OCV data from our specific type of cell. This calculation was done on both the charge and discharge steps and is shown as a plot in figure 6. Pseudo-OCV data was obtained by charging the cell SOC from 0% to 100% and then discharging the cell from 100% to 0% SOC at a slow rate of C/25 with a Maccor battery tester. This measurement was performed within a Binder thermal chamber held at 25 °C.

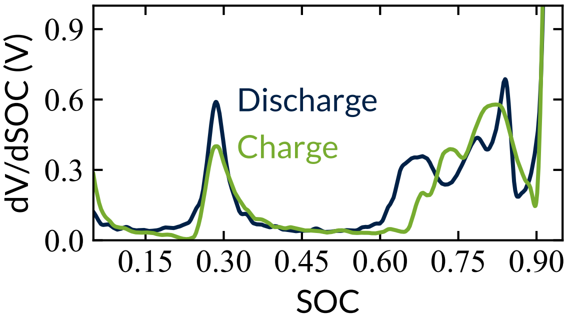

Figure 6 A plot of dV/dSOC for the pseudo-OCV curves from figure 5, used for k_U estimation.

Since the Biot number for this measurement configuration is small (~0.01) the time constant for the thermal response strongly depends on the heat transfer coefficient h, rather than the effective thermal diffusivity of the cell. Thus, the time constant of the average-temperature relaxation yields the heat transfer coefficient. In order to find optimal values of other thermal and electrochemical parameters, nonlinear least squares optimization was performed by fitting the periodic steady state data (from ~2000 s onwards) including cell voltage, minimum, maximum, and average temperatures for the 4c100s square-wave. The least squares routine in MATLAB (LSQNONLIN) was applied by integrating MATLAB's scripting environment with COMSOL Multiphysics' simulations via LiveLink for MATLAB. The cost function used for nonlinear least squares was taken to be

$$\begin{cases} \min\limits_{p} \left[\sum_{i=1}^{N} \left(\frac{V_{cell,i}^{\mathrm{m}} - V_{cell,i}^{exp}}{V_{cell,i}^{\mathrm{m}}} \right)^2 + \left(\frac{T_{max,i}^{\mathrm{m}} - T_{max,i}^{exp}}{T_{max,i}^{\mathrm{m}}} \right)^2 + \left(\frac{T_{avg,i}^{\mathrm{m}} - T_{avg,i}^{exp}}{T_{avg,i}^{\mathrm{m}}} \right)^2 + \left(\frac{T_{min,i}^{\mathrm{m}} - T_{min,i}^{exp}}{T_{min,i}^{\mathrm{m}}} \right)^2 \right] \\ p^l \leq p \leq p^u \end{cases} \tag{25}$$

where superscript m and exp represent the modeling and the experimental results, and p^{l} and p^{u} are the lower and upper bounds for the parameters, respectively. N represents the number of time steps simulated.

To capture the unsteady initial transient behavior as well as the periodic steady state, the ionic conductivity and exchange current density were assumed to change with temperature linearly and exponentially, respectively:

$$\kappa_e(T) = \kappa_e^{\infty} + \alpha_{\kappa_e}(T - T_{\infty}) \tag{26}$$

$$i_0(T) = i_0^{\infty} \exp\left[-\frac{E_{i_0}}{R} \left(\frac{1}{T} - \frac{1}{T_{\infty}} \right) \right] \tag{27}$$

Here κ_e^{∞} and i_0^{∞} are the properties at ambient temperature, and E_{i_0} is the activation energy for the exchange current density. The temperature dependences of these two parameters were also represented in the dimensional analysis section through properties $\tilde{\rho}_{\mathrm{liq}}$ and $\tilde{\rho}_{\mathrm{k}}$ (note that $\rho_k = a_V RT / i_0 nF$). This added thermal effect on the parameters is necessary to explain the gradual decrease in voltage envelope during cycling: in all experiments, it was found that the maximum variation of voltage ΔV_{T} decreased over time as the system evolved toward its periodic steady state, and this decrease correlated precisely with the average temperature.

The reported average temperature is a surface average, which was evaluated both experimentally and in simulations by integrating the temperature distribution across the whole surface, then dividing by the surface area. Experimentally, it was observed that the locations of the maximum and minimum temperatures did not change with time after a relatively early relaxation period. To simplify the work associated with experimental data processing, the locations of the maximum and minimum spots were fixed; only those small areas of the images were probed to evaluate the maximum and minimum temperatures. A spot size of five pixels by five pixels (corresponding to ~88 mm^2 on the battery surface) was ultimately used to gather thermal data around the hot and cold spots.

As previously mentioned, the number of layers in the cell was estimated to be 40. However, our implementation of scaling within the model allows this to be represented by one layer with 40 times the true thickness. This is justified as long as the Biot number is low (so the internal temperature of the cell is uniform), and other parameters are scaled to reflect the geometric adjustment. To further simplify the problem, a separator domain has not been explicitly included in the model equations. The consequences of this choice will be discussed in the following results section.

The copper bars that were used to connect the battery to the power supply were also simulated within the COMSOL model, by including them in the 3-D geometry. This was necessary because the bars act as a heat sink, which removes some of the heat generated within the small metal tabs. An enlarged 3-D representation of the geometry and the spatial mesh that was used for simulations is shown in figure 7. In the schematics, the through-plane thickness has been multiplied by ten to ease visualization of the relative thicknesses of the different simulation domains. The COMSOL file and MATLAB codes used to solve the model and implement the optimization are available on GitHub [43].

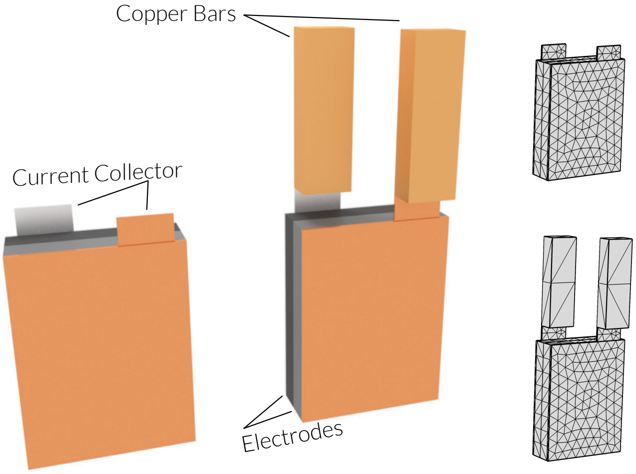

Figure 7 Geometry and mesh that were implemented in COMSOL for the simulations. The copper bars were added to more closely mimic the experimental setup.

6. Results and Discussion

Figure 8 compares the model output with the experimental results from three different excitation tests of the A123 prismatic cell. The first test and also the chosen experiment for fitting was the 4c100s square-wave, which is shown as the first set of plots in figure 8. The extracted parameter set shown in table 2 was obtained by fitting the model to the experimental data set with the most strenuous 4c100s input signal at 30% SOC. By using the extracted parameter set as new inputs for the COMSOL simulation, the model was then used to predict the behavior under other control conditions. Minor adjustments were made to reflect changes in ambient and operating conditions: for instance, material properties κ_e^{∞} and i_0^{∞} were adjusted to represent the values at the ambient temperatures in which experiments were performed. With these corrections, the model was then validated by comparing the model output with two different experiments, one with a different C rate and similar period (2c100s), and one with the same C rate and a different period (4c50s). The results of these two validation tests are shown in figure 8b and 8c.

The simulation matches the thermal response as well as the electrical response. The match supports the assertion that a simple thermo-electrochemical model based on Newman–Tobias theory with linear kinetics suffices to model the whole pouch cell. The fitted and corrected parameters are listed in table 2, while fixed parameters are listed in table 1. For a_V, the value is only applicable to the electrodes and not to the metal current collectors. For k_{eff}, only the metal outer layers take fixed values, while the electrodes' conductivity is optimized. Most parameter values fall within the range reported in literature. A notable exception is κ_e^∞, whose extracted value is ~0.02 $\frac{S}{m}$, while typically reported values are 0.1 – 1.0 $\frac{S}{m}$. This discrepancy likely owes to the fact that a separator layer was not explicitly included, which should decrease the effective conductivity observed.

The parameterization was also implemented for a few data sets centered around 50% and 70% SOC; corresponding data are also reported in table 2. Most parameters again matched literature values well, with the exception of κ_e^∞. For 30% SOC, the k_{U} value of 0.36 V is close to the measured value at 30% SOC (~0.33 V on charge and ~0.40 V on discharge). In the 50% SOC scenario, the extracted k_{U} value was 0.22 V, however, *vs*. the measured value of ~0.035 V on charge and discharge. This could imply that the current model cannot accommodate for chemistries with large plateaus in their OCV curves without the inclusion of extra physics. Nevertheless, five out of the seven model parameters did not change significantly across the three different charge states used as reference points. As expected, the remaining two, k_u and $\Delta\bar{S}_{\text{rxn}}$, whose values derive from derivatives of the OCV, do change with mean SOC.

Parameters	**Electrodes**	**Current Collectors/tabs**
thickness(mm)	2.7	0.4
width(mm)	150	48
height(mm)	200	25
a_V (1/m)	10^7	N/A
k_{eff} (W/m K)	-	380
κ_s (S/m)	50	10^7

Table 1. Electrode and current collector fixed parameters used in the model.

Parameters	**30%**	**50%**	**70%**	**Literature/Measured Value**
$h(\mathrm{W/m^2K})$	12.5	10.6	10.4	3-20 [42,44]
$C_{p,eff}(\mathrm{J/m^3K})$	2.32×10^6	2.04×10^6	2.09×10^6	1×10^6-3.5×10^6 [21,31]
$\Delta\bar{S}_{rxn}/nF(\mathrm{mV/K})$	-0.14	0.08	0.10	|0.01-1| [32,45]
$i_0(\mathrm{A/m^2})$ at 25 °C	$i_0^\infty(\mathrm{A/m^2}) = 14.31$ $E_{i_0}(\mathrm{KJ/mol}) = 30.81$	11.99 30.61	11.89 28.75	0.01-50[22] 1-50[22]
$\kappa_e(\mathrm{S/m})$ at 25 °C	$\kappa_e^\infty(\mathrm{S/m}) = 0.022$ $\alpha_{\kappa_e}(\mathrm{S/m/K}) = 0.002$	0.019 0.002	0.022 0.003	0.1-1[25,41]
$k_{eff}(\mathrm{W/mK})$	54.4	72.0	60.1	5-380[21]
$k_U(\mathrm{V})$	0.36	0.22	0.17	30%: 0.33-0.40 50%: 0.03-0.035 70%: 0.21-0.31

Table 2. Parameter values for fitting the 4c100s square-wave data. The modified values were implemented to recreate a reasonable reaction distribution in the porous electrode after simplifying its geometry.

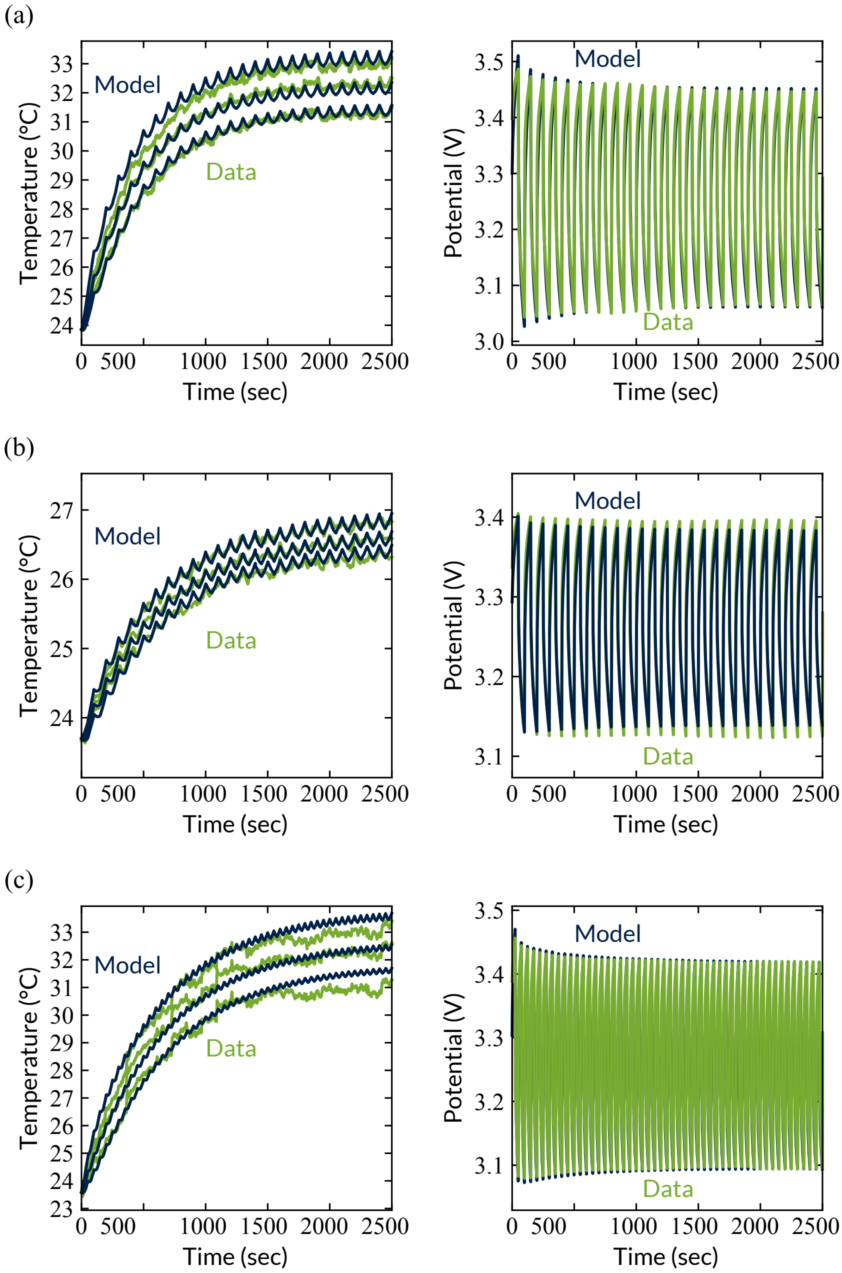

Figure 8 Comparison of model output and experimental data for three different excitation tests of the A123 prismatic cell for (a) 4c100s, (b) 2c100s, and (c) 4c50s input signals. The plots in (a) were the result of data fitting, while (b) and (c) were validation tests obtained by using the parameter set from (a).

7. Conclusion

A thermo-electrochemical model that modifies the isothermal Newman–Tobias model to account for a local thermal energy balance was developed and used to match experimental temperature-distributions as well as the voltage data for a 20 Ah LFP pouch cell from A123. Dimensional analysis showed that seven dimensionless variables control the output of a 3-D simulation with a square-wave-current excitation test, and that the simulation can be simplified to use fewer layers by rescaling certain model parameters so long as the Biot number is low. The non-uniform temperature distribution on the cell surface owes to the fact that cells have been designed for ease of wiring, with both tabs on the same edge of the cell, rather than to achieve a uniform internal current distribution. The nonuniformity of temperature is useful, however, because it can be gauged to obtain estimates of internal material properties. Using an iterative procedure based on a numerically computed goal-seeking algorithm, material properties were estimated for an A123 20 Ah LFP battery. It was also shown that the model had extrapolative capability; best-fit parameters obtained from a simulation fit at a high C rate could be used to predict the outputs at a different lower C rate or at a different frequency.

8. Acknowledgments

This work was supported by the US Army TARDEC Automotive Research Center, the US Department of Energy Advanced Research Projects Agency-Energy (ARPA-E), award number DE-AR0000269, and the EPSRC, grant no. EP/R020973/1.

Bibliography

[1] K.H. Kwon, C.B. Shin, T.H. Kang, C.-S. Kim, A two-dimensional modeling of a lithium-polymer battery, J. Power Sources. 163 (2006) 151–157.

[2] G.-H. Kim, K. Smith, K.-J. Lee, S. Santhanagopalan, A. Pesaran, Multi-domain modeling of lithium-ion batteries encompassing multi-physics in varied length scales, J. Electrochem. Soc. 158 (2011) A955–A969.

[3] U.S. Kim, J. Yi, C.B. Shin, T. Han, S. Park, Modeling the dependence of the discharge behavior of a lithium-ion battery on the environmental temperature, J. Electrochem. Soc. 158 (2011) A611–A618.

[4] U.S. Kim, J. Yi, C.B. Shin, T. Han, S. Park, Modelling the thermal behaviour of a lithium-ion battery during charge, J. Power Sources. 196 (2011) 5115–5121.

[5] S. Peck, M. Pierce, Development of a Temperature-Dependent Li-ion Battery Thermal Model, SAE Technical Paper, 2012.

[6] P. Ramadass, B. Haran, R. White, B.N. Popov, Mathematical modeling of the capacity fade of Li-ion cells, J. Power Sources. 123 (2003) 230–240.

[7] R. Ben Wright, C.G. Motloch, J.R. Belt, J.P. Christophersen, C.D. Ho, R.A. Richardson, I. Bloom, S.A. Jones, V.S. Battaglia, G.L. Henriksen, Calendar-and cycle-life studies of advanced technology development program generation 1 lithium-ion batteries, J. Power Sources. 110 (2002) 445–470.

[8] M.W. Verbrugge, R.S. Conell, Electrochemical and thermal characterization of battery modules commensurate with electric vehicle integration, J. Electrochem. Soc. 149 (2002) A45–A53.

[9] X. Lin, H.E. Perez, J.B. Siegel, A.G. Stefanopoulou, Y. Li, R.D. Anderson, Y. Ding, M.P. Castanier, Online Parameterization of Lumped Thermal Dynamics in Cylindrical Lithium Ion Batteries for Core Temperature Estimation and Health Monitoring, IEEE Trans. Control Syst. Technol. 21 (2013) 1745–1755. https://doi.org/10.1109/TCST.2012.2217143.

[10] H.E. Perez, J.B. Siegel, X. Lin, A.G. Stefanopoulou, Y. Ding, M.P. Castanier, Parameterization and validation of an integrated electro-thermal cylindrical lfp battery model, in: ASME 2012 5th Annu. Dyn. Syst. Control Conf. Dyn. Syst. Control Div. ASME, 2012: pp. 41–50.

[11] Y. Kim, J.B. Siegel, A.G. Stefanopoulou, A computationally efficient thermal model of cylindrical battery cells for the estimation of radially distributed temperatures, in: Am. Control Conf. ACC 2013, IEEE, 2013: pp. 698–703.

[12] Y. Kim, S. Mohan, J.B. Siegel, A.G. Stefanopoulou, Y. Ding, The estimation of temperature distribution in cylindrical battery cells under unknown cooling conditions, IEEE Trans. Control Syst. Technol. 22 (2014) 2277–2286.

[13] J. Christensen, D. Cook, P. Albertus, An Efficient Parallelizable 3D Thermoelectrochemical Model of a Li-Ion Cell, J. Electrochem. Soc. 160 (2013) A2258–A2267. https://doi.org/10.1149/2.086311jes.

[14] M. Doyle, T.F. Fuller, J. Newman, Modeling of Galvanostatic Charge and Discharge of the Lithium/Polymer/Insertion Cell, J. Electrochem. Soc. 140 (1993) 1526–1533. https://doi.org/10.1149/1.2221597.

[15] T.F. Fuller, M. Doyle, J. Newman, Simulation and Optimization of the Dual Lithium Ion Insertion Cell, J. Electrochem. Soc. 141 (1994) 1–10. https://doi.org/10.1149/1.2054684.

[16] T.F. Fuller, M. Doyle, J. Newman, Relaxation Phenomena in Lithium-Ion-Insertion Cells, J. Electrochem. Soc. 141 (1994) 982–990. https://doi.org/10.1149/1.2054868.

[17] S.U. Kim, P. Albertus, D. Cook, C.W. Monroe, J. Christensen, Thermoelectrochemical simulations of performance and abuse in 50-Ah automotive cells, J. Power Sources. 268 (2014) 625–633.

[18] S.U. Kim, C.W. Monroe, Increasing the rate capability of batteries with electrolyte flow, Appl. Energy. 103 (2013) 207–211.

[19] J. Liu, C.W. Monroe, Solute-volume effects in electrolyte transport, Electrochimica Acta. 135 (2014) 447–460.

[20] J.S. Newman, C.W. Tobias, Theoretical Analysis of Current Distribution in Porous Electrodes, J. Electrochem. Soc. 109 (1962) 1183–1191.

[21] V. Srinivasan, C.Y. Wang, Analysis of Electrochemical and Thermal Behavior of Li-Ion Cells, J. Electrochem. Soc. 150 (2003) A98–A106. https://doi.org/10.1149/1.1526512.

[22] M. Guo, G. Sikha, R.E. White, Single-Particle Model for a Lithium-Ion Cell: Thermal Behavior, J. Electrochem. Soc. 158 (2011) A122–A132. https://doi.org/10.1149/1.3521314.

[23] K. Kumaresan, G. Sikha, R.E. White, Thermal model for a Li-ion cell, J. Electrochem. Soc. 155 (2008) A164–A171.

[24] N. Nieto, L. Díaz, J. Gastelurrutia, I. Alava, F. Blanco, J.C. Ramos, A. Rivas, Thermal modeling of large format lithium-ion cells, J. Electrochem. Soc. 160 (2013) A212–A217.

[25] E. Prada, D. Di Domenico, Y. Creff, J. Bernard, V. Sauvant-Moynot, F. Huet, Simplified Electrochemical and Thermal Model of LiFePO4-Graphite Li-Ion Batteries for Fast Charge Applications, J. Electrochem. Soc. 159 (2012) A1508–A1519. https://doi.org/10.1149/2.064209jes.

[26] M. Xu, Z. Zhang, X. Wang, L. Jia, L. Yang, Two-dimensional electrochemical–thermal coupled modeling of cylindrical LiFePO 4 batteries, J. Power Sources. 256 (2014) 233–243.

[27] M. Fleckenstein, O. Bohlen, M.A. Roscher, B. Bäker, Current density and state of charge inhomogeneities in Li-ion battery cells with LiFePO 4 as cathode material due to temperature gradients, J. Power Sources. 196 (2011) 4769–4778.

[28] D. Bernardi, E. Pawlikowski, J. Newman, A general energy balance for battery systems, J. Electrochem. Soc. 132 (1985) 5–12.

[29] C. Forgez, D.V. Do, G. Friedrich, M. Morcrette, C. Delacourt, Thermal modeling of a cylindrical LiFePO 4/graphite lithium-ion battery, J. Power Sources. 195 (2010) 2961–2968.

[30] S. Al Hallaj, R. Venkatachalapathy, J. Prakash, J.R. Selman, Entropy changes due to structural transformation in the graphite anode and phase change of the LiCoO2 cathode, J. Electrochem. Soc. 147 (2000) 2432–2436.

[31] H. Maleki, S. Al Hallaj, J.R. Selman, R.B. Dinwiddie, H. Wang, Thermal Properties of Lithium-Ion Battery and Components, J. Electrochem. Soc. 146 (1999) 947–954.

[32] K.E. Thomas, C. Bogatu, J. Newman, Measurement of the entropy of reaction as a function of state of charge in doped and undoped lithium manganese oxide, J. Electrochem. Soc. 148 (2001) A570–A575.

[33] K.E. Thomas, J. Newman, Thermal Modeling of Porous Insertion Electrodes, J. Electrochem. Soc. 150 (2003) A176–A192. https://doi.org/10.1149/1.1531194.

[34] K.E. Thomas, J. Newman, Heats of mixing and of entropy in porous insertion electrodes, J. Power Sources. 119–121 (2003) 844–849. http://dx.doi.org/10.1016/S0378-7753(03)00283-0.

[35] M.R. Zakin, R.O. Brickman, D.M. Cox, A. Kaldor, Dependence of metal cluster reaction kinetics on charge state. I. Reaction of neutral (Nb_x) and ionic (Nb^+_x, Nb^-

$_x$) niobium clusters with D $_2$, J. Chem. Phys. 88 (1988) 3555–3560. https://doi.org/10.1063/1.453903.

[36] T.M. Bandhauer, S. Garimella, T.F. Fuller, A Critical Review of Thermal Issues in Lithium-Ion Batteries, J. Electrochem. Soc. 158 (2011) R1–R25.

[37] W.M. Deen, Analysis of Transport Phenomena, OUP USA, 2012.

[38] M. Doyle, Y. Fuentes, Computer Simulations of a Lithium-Ion Polymer Battery and Implications for Higher Capacity Next-Generation Battery Designs, J. Electrochem. Soc. 150 (2003) A706–A713. https://doi.org/10.1149/1.1569478.

[39] J. Newman, K.E. Thomas-Alyea, Electrochemical Systems, Wiley, 2012.

[40] S.G. Stewart, Determination of transport properties and optimization of lithium-ion batteries, University of California, Berkeley, 2007.

[41] J. Liu, C.W. Monroe, On the characterization of battery electrolytes with polarization cells, Electrochimica Acta. 167 (2015) 357–363. https://doi.org/10.1016/j.electacta.2015.03.104.

[42] X. Zhang, R. Klein, A. Subbaraman, S. Chumakov, X. Li, J. Christensen, C. Linder, S.U. Kim, Evaluation of convective heat transfer coefficient and specific heat capacity of a lithium-ion battery using infrared camera and lumped capacitance method, J. Power Sources. 412 (2019) 552–558.

[43] H.N. Chu, howiechu/lock-in-thermography-model: Electrochemical Thermal Model, 2019. https://doi.org/10.5281/zenodo.3369805.

[44] R.B. Bird, E.N. Lightfoot, W.E. Stewart, Transport Phenomena, Wiley, 2002.

[45] S.J. Bazinski, X. Wang, The Influence of Cell Temperature on the Entropic Coefficient of a Lithium Iron Phosphate (LFP) Pouch Cell, J. Electrochem. Soc. 161 (2014) A168–A175. https://doi.org/10.1149/2.082401jes.